

# Studying the Lyman- $\alpha$ optical depth fluctuations at $z \sim 5.5$ using fast semi-numerical methods

T. Roy Choudhury<sup>1\*</sup>, Aseem Paranjape<sup>2†</sup> and Sarah E. I. Bosman<sup>3</sup>

<sup>1</sup>National Centre for Radio Astrophysics, TIFR, Post Bag 3, Ganeshkhind, Pune 411007, India

<sup>2</sup>Inter-University Center for Astronomy & Astrophysics, Post Bag 4, Ganeshkhind, Pune 411007, India

<sup>3</sup>Department of Physics and Astronomy, University College London, London, UK

## ABSTRACT

We present a computationally efficient and fast semi-numerical technique for simulating the Lyman- $\alpha$  ( $\text{Ly}\alpha$ ) absorption optical depth in presence of neutral hydrogen “islands” leftover from reionization at redshifts  $5 \lesssim z \lesssim 6$ . The main inputs to the analysis are (i) a semi-numerical photon-conserving model of ionized regions during reionization (named **SCRIPT**) and (ii) the fluctuating Gunn-Peterson approximation to model the  $\text{Ly}\alpha$  absorption. Our model is then used for simulating the large-scale fluctuations in the effective optical depth as observed along sight lines towards high- $z$  quasars. We find that the model, with fiducial choice of free parameters, is in agreement with the results from more detailed radiative transfer simulations. By varying the free parameters, we obtain the constraints on reionization history at  $5 \lesssim z \lesssim 6$  as allowed by the data. We confirm that reionization is *not* complete before  $z \sim 5.6$  and the completion can be as late as  $z \sim 5.2$  (both within  $2 - \sigma$ ), the exact limits depending on how the non-detections of the flux in the data are treated. With further improvements in the model and with more sight lines at  $z \sim 6$ , we can take advantage of the computational efficiency of our analysis to obtain more stringent constraints at the tail-end of reionization.

**Key words:** galaxies: evolution – galaxies: high-redshift – galaxies: luminosity function, mass function

## 1 INTRODUCTION

The detection of quasars at high redshifts  $z \sim 6$  enabled a novel way of studying the end stages of reionization of neutral hydrogen (HI) by the early star formation (Fan et al. 2000, 2001, 2002, 2003, 2004; Songaila 2004; Fan et al. 2006a,b). The Lyman- $\alpha$  ( $\text{Ly}\alpha$ ) absorption spectra of these quasars are expected to contain information on the distribution of HI in the intergalactic medium (IGM) along the lines of sight. These observations of the  $\text{Ly}\alpha$  optical depth, combined with high-quality numerical simulations, allowed one to estimate the HI photoionization rate  $\Gamma_{\text{HI}}$  and thus the number of ionizing photons available in the IGM (Fan et al. 2006b; Bolton & Haehnelt 2007; Calverley et al. 2011; Wyithe & Bolton 2011). More detailed studies of these spectra based on, e.g., the damping wings and near zones (Wyithe & Loeb 2004; Maselli et al. 2007; Bolton & Haehnelt 2007; Wyithe & Bolton 2011; Bolton et al. 2011; Greig et al. 2017; Eilers et al. 2017, 2018b; Durovčková et al. 2020; Davies et al. 2020), evolution of the IGM tem-

perature (Raskutti et al. 2012; Boera et al. 2019), fraction of “dark” pixels in the spectra (McGreer et al. 2011, 2015), dark gap statistics (Songaila & Cowie 2002; Gallerani et al. 2006, 2008), have revealed a wealth of information on reionization.

The constraints obtained on the global HI fraction from these studies were relatively straightforward to interpret and implement in semi-analytical models (Wyithe & Loeb 2003; Choudhury & Ferrara 2005; Pritchard et al. 2010; Mitra et al. 2011, 2012). When combined with other observations, e.g., the Thomson scattering optical depth of the Cosmic Microwave Background (CMB) photons (Hinshaw et al. 2013; Planck Collaboration et al. 2019), these models were able to constrain the reionization history to a significant extent. Being analytical or semi-analytical in nature, probing a wide range of parameter space was natural for these models and hence they could be coupled to advanced statistical techniques, e.g., Markov chain Monte Carlo (MCMC) (Mitra et al. 2011, 2012; Greig & Mesinger 2015; Greig et al. 2019). Overall, the data seemed to be consistent with a picture wherein the reionization was completed by  $z \sim 5.8$ .

More recently, the  $\text{Ly}\alpha$  effective optical depth  $\tau_{\text{eff}}$  of the quasar absorption spectra at  $5.5 < z < 6$ , when averaged

\* E-mail: tirth@ncra.tifr.res.in

† Email: aseem@iucaa.in

over large scales ( $50h^{-1}\text{cMpc}$ ), showed significant fluctuations (Becker et al. 2015; Bosman et al. 2018; Eilers et al. 2018a, 2019). These fluctuations could not be explained by simple models of uniform  $\Gamma_{\text{HI}}$  and thus led to various speculations which included, e.g., temperature fluctuations in the IGM (D’Aloisio et al. 2015), presence of an undetected population of faint quasars (Chardin et al. 2015, 2017), fluctuations in the mean free path  $\lambda_{\text{mfp}}$  of ionizing photons (Davies & Furlanetto 2016), presence of HI islands leftover from reionization (Kulkarni et al. 2019; Keating et al. 2019), shot noise in the placement of bright sources like quasars (Meiksin 2020). At present, the two models which seem to be most successful in explaining the data are (i) the model of Davies & Furlanetto (2016) based on  $\lambda_{\text{mfp}}$  fluctuations (albeit with somewhat shorter  $\lambda_{\text{mfp}}$  than is usually assumed) and (ii) the model where the reionization is not complete till  $z \sim 5.3$  and thus the IGM contains leftover HI islands (Kulkarni et al. 2019; Keating et al. 2019). Interestingly, one is yet to find a definitive method to distinguish between the two scenarios from the available data (Nasir & D’Aloisio 2019).

In case the  $\tau_{\text{eff}}$  fluctuations are indeed due to the neutral islands, then these fluctuations are directly probing the tail end of reionization. Hence these observations need to be taken into account while attempting to constrain the reionization history. Kulkarni et al. (2019) have modelled these neutral patches using high-resolution SPH simulations and a cosmological radiative transfer code. Such simulations are usually computationally expensive and hence are not suited for probing the parameter space. Using semi-analytical or semi-numerical models to constrain reionization has the advantage that one is able to identify all possible histories allowed by the data by varying the free parameters, and subsequently study the state of the IGM along with properties of the ionizing sources (e.g., cooling, feedback, escape of ionizing photons; Mitra et al. 2013, 2018). In case one wants to include the  $\tau_{\text{eff}}$  fluctuation data in such statistical analyses, it becomes imperative to devise ways to model the HI islands in a computationally efficient manner.

The main aim of this work is to build a model of reionization and Ly $\alpha$  forest at  $z \sim 5.5$  which is computationally efficient and hence can be used for parameter space exploration. To achieve this, we use a previously developed semi-numerical method to generate ionized regions, driven by Lyman-continuum photons from galaxies, within relatively low-resolution but large simulation volumes (Choudhury & Paranjape 2018). Once the distribution of the ionized (and neutral) regions are generated, we then model the Ly $\alpha$  optical depth of neutral hydrogen (as would be imprinted on spectra of background point sources such as quasars) using the so-called fluctuating Gunn-Peterson approximation (Croft et al. 1998). The resulting realizations of the quasar absorption spectra are then used for calculating the  $\tau_{\text{eff}}$  along large lines of sight so as to allow proper comparison with observations. Because of the simplifications employed, we need to introduce a few free parameters in the model, thus decreasing its predictive power as compared to radiative transfer simulations. The free parameters are either fixed to values that give results similar to what is found in the full numerical simulations or constrained by comparing the model predictions with the observational data, the latter being possible due to the computational efficiency of our algorithm. The end result of the analysis is that we ob-

tain the range in reionization histories at  $5 \lesssim z \lesssim 6$  that are statistically allowed by the data.

The paper is organized as follows: We discuss our method of calculating the Ly $\alpha$  optical depth in Section 2. In Section 3, we present the main results of our analysis before summarizing and discussing the future outlook in Section 4. The appendices are devoted to exploring the model parameters beyond their default values. The cosmological parameters used in this work are  $\Omega_m = 0.308$ ,  $\Omega_\Lambda = 1 - \Omega_m$ ,  $\Omega_b = 0.0482$ ,  $h = 0.678$ ,  $n_s = 0.961$ ,  $\sigma_8 = 0.829$  (Planck Collaboration et al. 2014).

## 2 METHOD

### 2.1 Generation of ionization maps using SCRIPT

The ionization maps needed for this work are generated using the semi-numerical method introduced in Choudhury & Paranjape (2018). The method consists of two steps. In the first, we use a collisionless  $N$ -body simulation to generate the large-scale smoothed density fields along with the large-scale distribution of the collapsed haloes. In the second step, the density and the halo fields are used as input to an explicitly photon-conserving semi-numerical formalism to generate the distribution of ionized regions.

For the  $N$ -body simulation, we use the publicly available code GADGET-2<sup>1</sup> (Springel 2005) and simulate a box of length  $256h^{-1}\text{cMpc}$  with  $512^3$  particles. The initial conditions for the simulation are generated using the N-GenIC code<sup>2</sup>. At redshifts of interest, the simulation output in the form of the particle positions are smoothed using a Cloud-in-Cell (CIC) algorithm to generate the matter overdensity field  $\Delta_i = \rho_i/\bar{\rho}$  in a uniform grid with cells labelled by  $i$ .

Since the particle resolution of our box is not sufficient to identify the collapsed haloes of interest, we employ a sub-grid scheme to compute the large-scale halo distribution from the density field. Given the overdensity field, we use the conditional mass function from ellipsoidal collapse (Sheth & Tormen 2002), with parameters calibrated to match simulation results, to generate the fraction of mass  $f_{\text{coll},i}$  in collapsed haloes above a mass  $M_{\text{min}}$  inside every grid cell. Note that this approximate way of computing the collapsed mass works only for relatively larger grid volumes, hence we do not use grids finer than  $2h^{-1}\text{cMpc}$ . Our method not only produces the halo mass function consistent with  $N$ -body simulations (Jenkins et al. 2001), but also the large-scale clustering of haloes.

The generation of ionization maps requires computing two numbers in every cell in the box. The first is the number of hydrogen atoms which is assumed to follow the dark matter at scales of our interest

$$N_{H,i} = \bar{n}_H V_{\text{cell}} \Delta_i, \quad (1)$$

where  $\bar{n}_H$  is the mean comoving hydrogen number density and  $V_{\text{cell}}$  is the comoving volume of the grid cells. Secondly, we need the cumulative number of ionizing photons produced, which can be assumed to be proportional to the mass

<sup>1</sup> <https://wwwmpa.mpa-garching.mpg.de/gadget/>

<sup>2</sup> <https://wwwmpa.mpa-garching.mpg.de/gadget/right.html#ICcode>

within collapsed haloes above a mass  $M_{\min}$  and is given by

$$N_{\text{ion},i} = \zeta N_{H,i} f_{\text{coll},i} = \zeta \bar{n}_H V_{\text{cell}} \Delta_i f_{\text{coll},i}, \quad (2)$$

where  $\zeta$  is the ionizing efficiency.

The ionization maps are generated using the photon-conserving semi-numerical scheme introduced in Choudhury & Paranjape (2018), which is named SCRIPT (Semi-numerical Code for ReIonization with PhoTon-conservation). This method includes several improvements over existing semi-numerical codes based on the excursion-set formalism, namely, (i) it conserves the number of ionizing photons thus fixing a known shortcoming of earlier models (see, e.g., Zahn et al. 2007; Paranjape et al. 2016), and (ii) consequently ensures the numerical convergence of large-scale properties of the ionization field with respect to the resolution at which the maps are made. The code has recently been optimized so that it runs in 2 – 4 seconds on a single processor for a  $128^3$  grid.

In this work, we choose  $M_{\min} = 10^9 M_{\odot}$  which is appropriate for late stages of reionization. At these redshifts, most regions are photoheated and hence the star-formation threshold is set by the radiative feedback. We have also varied  $M_{\min}$  in the range  $10^8 - 10^{10} M_{\odot}$  and found that the Ly $\alpha$  optical depth statistics (to be introduced and discussed later) are insensitive to the value of  $M_{\min}$  as long as the value of global ionization volume fraction  $Q_{\text{HI}}^V$  remains fixed.

## 2.2 Calculation of the photoionization rate within ionized regions

The output of the semi-numerical method described above provides the neutral hydrogen fraction  $x_{\text{HI}}$  for each cell which can, in principle, be zero in regions that are completely ionized. In reality, however, the recombinations will ensure that there exist some residual neutral atoms even in these cells. The fraction of such neutral atoms would be exceedingly small (unless they are in high-density self-shielded regions) and hence would hardly affect the large-scale properties of the 21 cm signal. On the other hand, for studying the quasar spectra, this residual neutral hydrogen in the low-density IGM would cause the Ly $\alpha$  absorption observed in quasar spectra and hence needs to be modelled properly.

The main ingredient in modelling the residual neutral fraction is the photoionization rate  $\Gamma_{\text{HI}}$ . In order to do so, let us start with the flux incident on the  $i$ th cell

$$J_i(\nu) = \sum_{j \neq i} \frac{L_j(\nu)}{(4\pi)^2 (a x_{ij})^2} e^{-\tau_{ij}(\nu)}, \quad (3)$$

where  $L_j(\nu)$  is the luminosity of the  $j$ th cell,  $x_{ij}$  is the *co-moving* distance between the  $i$ th and the  $j$ th cells and  $\tau_{ij}$  is the optical depth between the two cells. The summation extends over all cells other than the cell under consideration. The optical depth between the two cells  $i$  and  $j$  can be calculated by integrating along the sightline joining the cell (Davies & Furlanetto 2016)

$$\tau_{ij}(\nu) = \int_{x_i}^{x_j} \frac{dx}{\lambda_{\text{mfp}}(\nu, x)}. \quad (4)$$

As shown in Davies & Furlanetto (2016), computing the mean free path self-consistently requires iterative solutions and can be computationally expensive (Hutter 2018). To start with, for ionized regions, we can make the simplifying

assumption that the mean free path takes just one value for the whole box. This approximation is believed to be adequate in the post-reionization universe where the value of  $\lambda_{\text{mfp}}$  is determined by the distance between the self-shielded regions. Let us denote this mean free path by  $\lambda_{\text{ss}}$ . This approximation is probably acceptable also for cells within an ionized region as long as its size is significantly larger than  $\lambda_{\text{mfp}}$ . However, the assumption breaks down at early stages of reionization where the mean free path is pre-dominantly determined by the bubble size. The assumption may also not hold good at later stages of reionization for cells close to the boundaries of the ionized regions as these cells do not receive contribution from sources in the direction of the neutral regions. In the excursion set-based semi-numerical models, a possible solution is to use  $\lambda_{\text{mfp}} = \min[\lambda_{\text{ss}}, \lambda_{\text{bub}}]$ , where  $\lambda_{\text{bub}}$  is the largest filtering scale at which the cell becomes ionized and hence is a measure of the bubble size (Hutter 2018).

We too adopt a similar approach to estimate the mean free path except that in our photon-conserving scheme, there is no concept of such filtering scales. Instead, we estimate the bubble size from the ionization maps using the spherical averaging method (Zahn et al. 2007). This method consists of constructing spheres around every cell in the box, averaging the ionized fraction within these spheres and then finding the largest such sphere for which the average ionized fraction is above a pre-determined threshold value  $x_{\text{th}}$ . The radius of the largest sphere is an estimate of the bubble size  $\lambda_{\text{bub},i}$  around the cell and hence, we take the mean free path to be

$$\lambda_{\text{mfp},i} = \min[\lambda_{\text{ss}}, \lambda_{\text{bub},i}]. \quad (5)$$

The mean free path in our model can vary substantially across the box at the early stages of reionization. At later stages (in particular at the tail end of reionization), the mean free path for most of the cells is given by a single  $\lambda_{\text{ss}}$  except for the cells close to the boundaries of the ionized regions where  $\lambda_{\text{bub},i}$  can end up being smaller. The mean free path is also taken to be independent of  $\nu$ . This is reasonable because the dependence is relatively weak and hence does not have a significant effect in the  $\nu$ -integration which anyway contains terms of steep  $\nu$ -dependence.

We next propagate the inhomogeneity of the mean free path into the optical depth (4) by only considering the dependence of  $\lambda_{\text{mfp}}$  on *the cell under consideration*, leading to

$$\tau_{ij} = \frac{x_{ij}}{\lambda_{\text{mfp},i}}. \quad (6)$$

This ansatz focuses on the cell in question and effectively penalises all sources that happen to lie farther from this cell than the nearest neutral region. This is clearly only an approximation, since it ignores all direction dependence in the placement of neutral islands and sources around the cell in question. However, our method still gives lower fluxes at cells that are close to the neutral islands and hence are likely to be affected by shadowing. The advantage of the method is that it is computationally much faster than any method that depends on lines of sight.

The luminosity  $L_i(\nu)$  is related to the quantity  $N_{\text{ion},i}$  used for generating the ionization maps in Section 2.1. However, since  $N_{\text{ion},i}$  is the cumulative number of photons pro-

duced, we need to introduce a characteristic time-scale  $t_*$  to relate it to the instantaneous luminosity. We can then write

$$L_i(\nu) = \dot{N}_i(\nu) h\nu \equiv \frac{N_i(\nu)}{t_*} h\nu, \quad (7)$$

where  $N_i(\nu)$  is simply the cumulative number of photons produced and is related to  $N_{\text{ion},i}$  by

$$N_{\text{ion},i} = \int_{\nu_{\text{HI}}}^{\infty} d\nu N_i(\nu), \quad (8)$$

where  $\nu_{\text{HI}}$  is the Lyman-limit frequency. The calculation then follows the usual approach outlined in [Davies & Furlanetto \(2016\)](#); [Hutter \(2018\)](#) and the photoionization rate can be shown to be given by

$$\Gamma_{\text{HI},i} = \frac{1}{a^2} \frac{\alpha}{\alpha + \beta} \frac{\sigma_{\text{HI}}(\nu_{\text{HI}})}{4\pi t_*} \sum_{j \neq i} N_{\text{ion},j} \frac{e^{-x_{ij}/\lambda_{\text{mfp},i}}}{x_{ij}^2}, \quad (9)$$

where  $\alpha$  is the spectral index of the ionizing sources,  $\beta$  is the spectral index of the hydrogen ionization cross section and  $\sigma_{\text{HI}}$  is the cross section at  $\nu = \nu_{\text{HI}}$ . The main advantage of our method of estimating  $\Gamma_{\text{HI},i}$  is that, since the above summation depends only on  $x_{ij}$ , it can be expressed as a sum over contributions from spherical shells around the  $i$ th cell and hence can be computed using spherical filters. This allows the calculation to be extremely efficient computationally.

A final point to note is that the above summation accounts only for the cells other than the cell under consideration. For the local contribution, we assume that the sources within  $\Delta R$  (the grid size) are distributed uniformly, hence the photoionization rate is given by ([Davies & Furlanetto 2016](#))

$$\Gamma_{\text{HI},i}^{\text{local}} = \frac{1}{a^2} \frac{\alpha}{\alpha + \beta} \frac{\sigma_{\text{HI}}(\nu_{\text{HI}})}{4\pi t_*} \times N_{\text{ion},i} \left[ 1 - e^{-\Delta R/\lambda_{\text{mfp},i}} \right] \frac{3\lambda_{\text{mfp},i}}{(\Delta R)^3}, \quad (10)$$

where  $\Delta R$  is the radius of the sphere corresponding to the grid volume. The final photoionization rate is calculated by adding this local contribution to the one computed using equation (9).

Our model of the photoionization rate thus requires the knowledge of three quantities (which are in general functions of  $z$ ). We discuss these parameters and their default choices below:

(i) The most important parameter is the threshold value  $x_{\text{th}}$  of ionized fraction required to identify the largest ionized sphere in the spherical averaging method. There is no way of determining this parameter rigorously from first principles within the scope of our model. We also found that  $x_{\text{th}}$  is highly degenerate with the global HI fraction, hence we cannot treat it as a free parameter while attempting to constrain the reionization history. We hence fix its value by demanding consistency of our model with existing simulations.

Note that the threshold  $x_{\text{th}}$  essentially determines how effective the neutral islands are in blocking the ionizing photons from reaching the other side. [Nasir & D’Aloisio \(2019\)](#) implement this effect in a more direct way by removing contributions from sources whose lines of sight pass through

neutral islands<sup>3</sup>. We find that we can match the observed  $\tau_{\text{eff}}$  distribution with a reionization history qualitatively similar to theirs (the `late-reion-long-mfp` model) if we choose  $x_{\text{th}} = 0.9$ <sup>4</sup>. We also find that with this choice of  $x_{\text{th}}$ , we can match the observations with a reionization history consistent with that used in [Kulkarni et al. \(2019\)](#); [Keating et al. \(2019\)](#). Interestingly, for most calculations of the bubble size during reionization at  $z \sim 7 - 8$ , e.g., [Zahn et al. \(2007\)](#); [Friedrich et al. \(2011\)](#), the value is taken to be  $x_{\text{th}} = 0.9$ .

We study in [Appendix A1](#) the effect of  $x_{\text{th}}$  on our results and how it affects the constraints on the inferred reionization history.

(ii) The next parameter is the mean free path  $\lambda_{\text{ss}}$  of ionizing photons as determined by the distance between the self-shielded regions. We choose its value as extrapolated from  $z \lesssim 5$  observations ([Worseck et al. 2014](#)) having the empirical power-law fitting form

$$\lambda_{\text{ss}}(z) = 175 \text{ cMpc} \left( \frac{1+z}{5.0} \right)^{-4.4}. \quad (11)$$

We study the effect of  $\lambda_{\text{ss}}$  values different from the above default choice in [Appendix A2](#).

(iii) The final parameter is the normalization factor to calculate the photoionization rate in equations (9) and (10)

$$A_{\Gamma} = \frac{\alpha}{\alpha + \beta} t_*^{-1}. \quad (12)$$

Depending on the objective, we either fix this parameter by matching the predicted mean transmitted flux with the data or treat it as a free parameter to be constrained by observations.

### 2.3 The Lyman- $\alpha$ optical depth

Having calculated the distribution of HI in the IGM, as caused by the Lyman-continuum photons from galaxies, we now compute the Ly $\alpha$  optical depth  $\tau_{\alpha}$  arising from the HI field. This  $\tau_{\alpha}$  field would get imprinted on the spectra of distant quasars which act as background sources.

For a cell that is identified as completely ionized by our semi-numerical model of reionization, the residual neutral hydrogen fraction is obtained assuming photoionization equilibrium

$$x_{\text{HI},i} \Gamma_{\text{HI},i} = \frac{\chi_{\text{He}}}{a^3} \alpha_B(T_i) n_{H,i} (1 - x_{\text{HI},i})^2, \quad (13)$$

where  $\chi_{\text{He}} \approx 1.08$  accounts for the excess electron produced by singly-ionized helium,  $\alpha_B(T)$  is the case-B recombination rate and the factor  $a^3$  accounts for the fact that the number densities used are in comoving units. The solution to the quadratic equation is straightforward provided we assume a relation between the temperature  $T_i$  of the cell and the

<sup>3</sup> The direct method of implementing the shadow of neutral islands ([Nasir & D’Aloisio 2019](#)) turns out to be computationally time-consuming in our simulations, hence we stick to a method that is approximate but computationally efficient.

<sup>4</sup> Note that we fix the reionization history by comparing with the data from [Bosman et al. \(2018\)](#), while [Nasir & D’Aloisio \(2019\)](#) compare their model with the data of [Eilers et al. \(2019\)](#). However, this should not have any significant effect on our chosen value of  $x_{\text{th}}$ .

density, which is usually taken to be a power-law  $T_i \propto \Delta_i^{\gamma-1}$  (although the relation could have significant scatter because of reionization, see below for a discussion). For most cases of interest, applying the above photoionization equilibrium equation to the completely ionized cells yields neutral fractions much smaller than unity which turn out to be

$$x_{\text{HI},i} \approx \frac{\chi_{\text{He}}}{a^3} \frac{\alpha_B(T_i) n_{\text{H},i}}{\Gamma_{\text{HI},i}}. \quad (14)$$

Under the fluctuating Gunn-Peterson approximation, the Ly $\alpha$  optical depth is given by

$$\tau_{\alpha,i} = \frac{\pi e^2}{m_e c} f_\alpha \lambda_\alpha H^{-1}(z) x_{\text{HI},i} n_{\text{H},i}, \quad (15)$$

where  $f_\alpha$  is the corresponding oscillator strength and all other symbols have their usual meanings. Hence, the dependence on the photoionization rate and other properties of the cell is given by

$$\tau_{\alpha,i} \propto \frac{\alpha_B(T_i) n_{\text{H},i}^2}{\Gamma_{\text{HI},i}} \propto \frac{\Delta_i^{2.7-0.7\gamma}}{\Gamma_{\text{HI},i}}, \quad (16)$$

where we have assumed  $\alpha_B(T) \propto T^{-0.7}$ .

In numerical simulations where reionization is assumed to be instantaneous and uniform, the value of  $\gamma$  is found to be around unity right after the reionization is completed and subsequently approaches a value  $\sim 1.5$  (Puchwein et al. 2015; Gaikwad et al. 2018). In reality, the temperature distribution could be more complicated given that different points in the IGM get reionized at different times and hence the  $T_i - \Delta_i$  relation is not necessarily one-to-one. Note that the value of  $\gamma$  used in the above applies to pixels that are ionized. If we make a simplifying assumption that a substantial fraction of them got ionized sufficiently early, we can take  $\gamma = 1.5$  in such regions<sup>5</sup>. Our method of fixing the value of  $\gamma$  is similar to what is done in other low-resolution simulations of the Ly $\alpha$  absorption (Davies & Furlanetto 2016).

The normalization constant in the above equation is completely degenerate with the unknown normalization  $A_\Gamma$  required to estimate the photoionization rate, and hence is absorbed in the definition of  $A_\Gamma$ . One should also keep in mind that the resolution of our simulations are rather coarse and hence our estimates of  $\tau_{\alpha,i}$  do not account for the small-scale fluctuations in the density and velocity fields. Such uncertainties are often accounted for by introducing an unknown normalization factor (Dixon & Furlanetto 2009; Davies & Furlanetto 2016) which can also be absorbed within  $A_\Gamma$ . Note that this implies that we cannot obtain the true value of  $\Gamma_{\text{HI}}$  from our low-resolution simulations, however, we assume that the fluctuations in the rate are

<sup>5</sup> In principle, the parameter  $\gamma$  could be treated as free and allow to be constrained by matching with the data. However, we found that it is highly degenerate with the normalization constant  $A_\Gamma$  and the constraints do not converge sufficiently well with the presently available data. The other option would be to solve the temperature evolution equation self-consistently in each pixel throughout the reionization history. This would require a significant extension of our present model, e.g., modelling the spectra of the reionization sources and including a prescription for the sub-grid clumping factor, which we plan to include in the future.

captured correctly. As mentioned earlier, the unknown normalization is either fixed by comparing with the observed mean transmitted flux or kept as a free parameter.

Note that the above relation is applied only to those cells which are identified as completely ionized by the semi-numerical method, whereas for cells that are partially or completely neutral, we assign the neutral fraction as obtained from the semi-numerical calculation itself.

The transmitted flux for the cell is given by  $e^{-\tau_{\alpha,i}}$ , hence the effective optical depth averaged over  $N$  pixels is given by

$$\tau_{\text{eff}} = -\ln \left[ \frac{1}{N} \sum_i e^{-\tau_{\alpha,i}} \right]. \quad (17)$$

This is the main observable in our work which will be compared with the observations.

## 2.4 Observational data

The main observational data used in this work is from Bosman et al. (2018) who have measured the Ly $\alpha$  effective optical depth  $\tau_{\text{eff}}$  averaged over  $50h^{-1}$  cMpc chunks in the redshift range  $5 \lesssim z \lesssim 6$ . We use their ‘GOLD’ sample which consists of spectra with various quality-cuts. Their results are presented as ‘optimistic’ and ‘pessimistic’ limits on the cumulative distribution function (CDF)  $P(< \tau_{\text{eff}})$  depending on how they treat the non-detections of the transmitted flux. In the optimistic case, the lower limits on  $\tau_{\text{eff}}$  are treated as measurements just below the detection sensitivity, while in the pessimistic case, these are assumed to have  $\tau_{\text{eff}} \rightarrow \infty$ .

## 3 RESULTS

### 3.1 The $\tau_{\text{eff}}$ distribution for a fiducial reionization history

Let us first check the ability of our model in matching the data and also the main features in terms of the physical quantities. As an illustrative case, we choose a reionization history which is broadly consistent with the very late model of Kulkarni et al. (2019). We use the default values  $x_{\text{th}} = 0.9$  and  $\lambda_{\text{ss}}$  evolving according to equation (11) while the normalization factor  $A_\Gamma$  is chosen so as to match the observed mean transmitted flux at each redshift bin (Bosman et al. 2018). For a given redshift, we compute the CDF  $P(< \tau_{\text{eff}})$  from our simulations by drawing as many random lines of sight of length  $50h^{-1}$  cMpc as there are in the observational data. We also make 500 realizations of the CDF to estimate the cosmic variance.

The predictions of  $P(< \tau_{\text{eff}})$  for the fiducial model and the match with the data are shown in Figure 1. The red curves denote  $P(< \tau_{\text{eff}})$  for the optimistic and pessimistic cases, respectively and the gray shaded regions denote the predictions of our model accounting for statistical fluctuations along different sight lines.

The first obvious point to note is that the model provides decent match to the data at all redshifts. The data at  $z = 5$  is consistent with a completely ionized medium and hence a uniform  $\Gamma_{\text{HI}}$ , which was also noted by Becker et al. (2015); Bosman et al. (2018). However, at higher redshifts

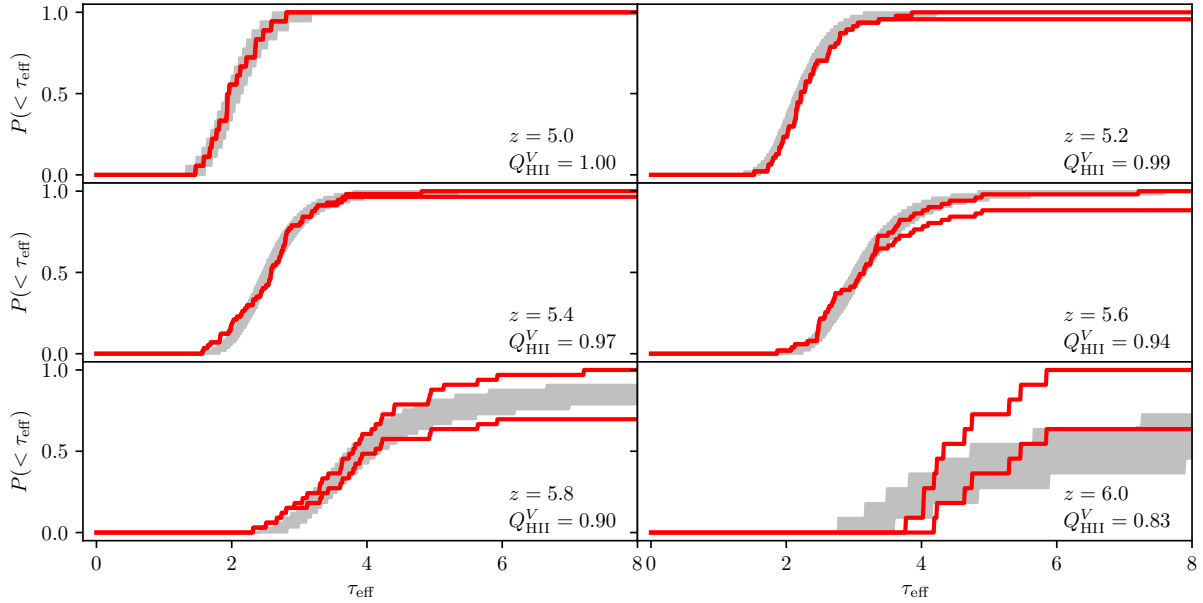


**Figure 1.** The cumulative  $\tau_{\text{eff}}$  distribution for the fiducial reionization model (see Section 3.1 for details). The two red curves show the observational data for the optimistic and pessimistic cases of [Bosman et al. \(2018\)](#). The gray shaded regions correspond to the model predictions accounting for statistical fluctuations along different sight lines. The redshifts and the ionized volume fractions  $Q_{\text{HII}}^V$  are mentioned in the respective panels.

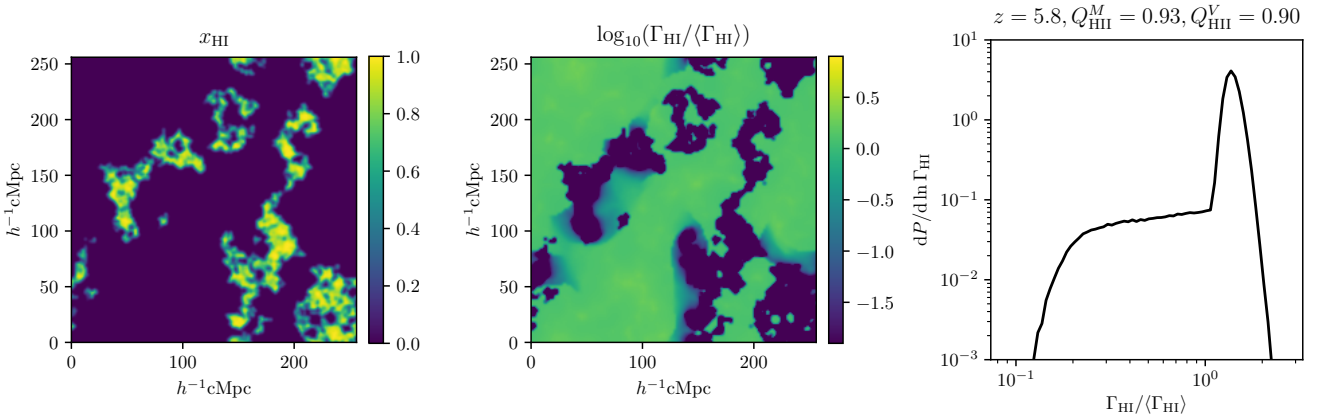


**Figure 2.** Various quantities obtained from our semi-numerical simulation at  $z = 5.8$  where the ionized volume fraction  $Q_{\text{HII}}^V = 0.9$  (the corresponding ionized mass fraction being  $Q_{\text{HII}}^M = 0.93$ ). The left hand panel shows the neutral hydrogen fraction  $x_{\text{HI}}$  field for a slice of thickness  $2h^{-1}\text{cMpc}$ , while the middle panel shows the  $\Gamma_{\text{HI}}$  fluctuations for the same slice. The right hand panel shows the PDF of  $\Gamma_{\text{HI}}$  for only points *in the ionized regions*.

we require the presence of some neutral patches in the IGM (characterized by a ionized volume fraction  $Q_{\text{HII}}^V < 1$ ) to match the data. The introduction of neutral islands in the model allows for sight lines with large  $\tau_{\text{eff}}$  which captures the high- $\tau_{\text{eff}}$  tail of the distribution. The match is seemingly worse at  $z = 6$  which could indicate that some of our model assumptions or the default choice of the parameters are breaking down. However, while evaluating the goodness of the match (say, by calculating the  $\chi^2$ , see below for details), we realize that the fiducial model is within the acceptable range (i.e.,  $\chi^2/\text{d.o.f} \sim 1$ ). Because of the small number of observed sight lines at  $z = 6$ , the statistical errors are

large and hence it becomes difficult to test the model assumptions critically.

Let us now understand the characteristics of the ionization and the radiation fields for our model. We choose  $z = 5.8$  where the effect of patchy reionization is most prominent. The results are shown in Figure 2. The left hand panel shows the neutral fraction  $x_{\text{HI}}$  map for a two-dimensional slice of thickness  $2h^{-1}\text{cMpc}$  while the middle panel shows the fluctuations in the photoionization rate  $\Gamma_{\text{HI}}$ . The ionization field resembles an almost ionized universe with patches of neutral islands in between. Also as expected,  $\Gamma_{\text{HI}}$  is more or less uniform in the ionized regions while it is zero in the neutral regions, thus tracing the overall topology of the ion-

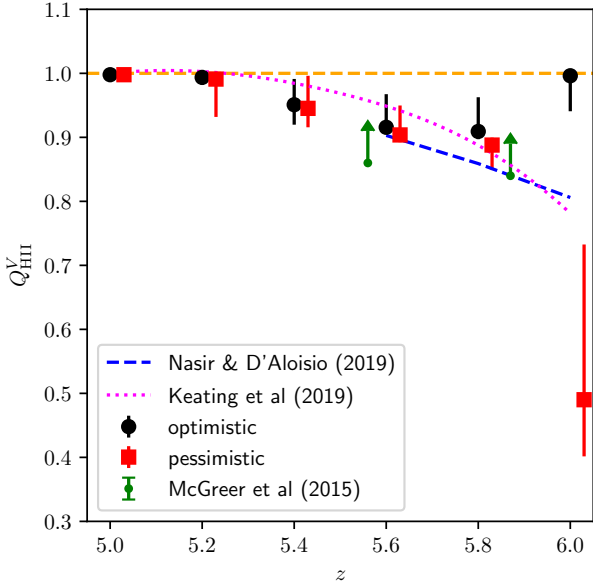


**Figure 3.** Constraints on  $Q_{\text{HII}}^V$  obtained from the MCMC analysis for the optimistic (black circles with error-bars) and pessimistic (red squares with error-bars, shifted slightly along the redshift axis for clarity) data sets of Bosman et al. (2018). The horizontal orange dashed line corresponds to  $Q_{\text{HII}}^V = 1$ . The blue dashed curve corresponds to the late-reion-long-mfp reionization history of Nasir & D’Aloisio (2019) while the magenta dotted curve is the the default reionization model of Keating et al. (2019). The green points with error-bars reflect the  $2 - \sigma$  lower limits on  $Q_{\text{HII}}^V$  obtained using the dark pixel fraction (McGreer et al. 2015).

ization map. What is interesting to note is that even in the ionized regions there are pixels very close to the neutral islands where the photoionization rate is quite small. These regions look like “shadows” in the map and arise because they do not receive photons from sources beyond the neutral islands. In our model, this effect is captured via the inclusion of the  $\lambda_{\text{bub}}$ , the scale above which the pixel under consideration begins to see the neutral cells.

To see the effect of these shadows on the distribution of  $\Gamma_{\text{HI}}$  in the ionized regions, we plot the PDF  $dP/d\ln\Gamma_{\text{HI}}$  (computed using only pixels in the ionized regions) in the right hand panel of Figure 2. One can see that there is a sharp distribution around the mean  $\Gamma_{\text{HI}}$ , however, there also exists a “knee”-like distribution for small values of  $\Gamma_{\text{HI}}$ . These points correspond to the shadows near the neutral islands. Our  $\Gamma_{\text{HI}}$  distribution can be compared with those of Davies & Furlanetto (2016); Nasir & D’Aloisio (2019) who find a low- $\Gamma_{\text{HI}}$  tail. In fact, Nasir & D’Aloisio (2019) have explicitly checked that such a tail arises from shadowing of the neutral islands. In this sense, our findings are qualitatively similar to theirs. However, the exact shape of the distributions are different. While theirs are a continuous bell-shaped distribution, ours show a sharp peak combined with a peculiar knee-like shape. The reason is that we use a simplifying assumption of a constant  $\lambda_{\text{ss}}$  in the ionized regions which lead to reduced fluctuations. These differences do not affect the results on  $P(< \tau_{\text{eff}})$  in any significant way.

### 3.2 Constraints on the reionization history

Now that we understand the main characteristics of our model, we utilize its efficiency to investigate the kind of constraints the  $\tau_{\text{eff}}$  fluctuations put on the reionization history. The main steps followed in the analysis are:

- We first convert the observational data on the CDF  $P(< \tau_{\text{eff}})$  to the differential PDF  $dP/d\tau_{\text{eff}}$ . Using the differential distribution for our analysis ensures that each measurement of  $\tau_{\text{eff}}$  from the observed spectra contributes to only one bin thus reducing correlations across different bins.
- The pessimistic and optimistic limits of Bosman et al. (2018) data differ in the way the non-detections of the transmitted flux are treated. In principle, one can take the forward modelling approach and use the noise characteristics of the telescopes to contaminate the simulated spectra appropriately. This will allow a fair comparison with the data without making any assumptions about the value of  $\tau_{\text{eff}}$  in case of non-detections. However, the features most affected while adding the noise are narrow transmission spikes ( $\lesssim$  cMpc across, see Chardin et al. 2018; Gaikwad et al. 2020) which are not resolved by the low-resolution pixels of our model. Hence we take a different approach where we treat the optimistic and pessimistic bounds as two independent data sets and compare them with the simulated spectra without adding any noise. Since the bounds provide reliable extrema for the recovery of the underlying distribution, the two sets of constraints thus obtained on the reionization history should bracket the full range of allowed histories.
- We treat each redshift bin as independent and vary  $Q_{\text{HII}}^V$  (by varying  $\zeta$  in the semi-numerical model) and the normalization  $A_{\Gamma}$  as two free parameters. We then constrain these two parameters by comparing the model predictions with the data (both for the pessimistic and the optimistic data sets) using a Bayesian likelihood method.

• The likelihood analysis requires computing the  $\chi^2$ , which in turn requires the error covariance matrix of  $dP/d\tau_{\text{eff}}$ . We estimate the covariance matrix from 500 independent realizations of the distribution from the simulation, accounting for correlations between different  $\tau_{\text{eff}}$  bins. For computational convenience, we compute the covariance matrix only for a fiducial set of  $Q_{\text{HII}}^V$  and  $A_{\Gamma}$  (for each redshift and each data set) and use it throughout the analysis. The fiducial parameter values are obtained by exploring the parameter space in a coarse grid and finding the set which gives a good match to the data.

• We use the publicly available affine-invariant ensemble sampler for Markov chain Monte Carlo (MCMC) called emcee (Foreman-Mackey et al. 2013) to obtain the posterior distribution of the parameters. We use flat priors on both  $Q_{\text{HII}}^V$  and  $A_{\Gamma}$  in the range  $[0, 1]$  and  $[0, \infty]$ , respectively. We use 20 walkers and run the chains long enough so that they converge, which is assessed through the auto-correlation analysis of Goodman & Weare (2010). The posterior distribution of  $Q_{\text{HII}}^V$  as a function of  $z$  provides us with the constraints on reionization history.

The best-fit values of  $Q_{\text{HII}}^V$  along with the  $2 - \sigma$  errors obtained from our likelihood analysis for the optimistic (black circles with error-bars) and pessimistic (red squares with error-bars, shifted slightly along the horizontal axis for clarity) cases are shown in Figure 3. The horizontal orange

dashed line corresponds to  $Q_{\text{HII}}^{\text{V}} = 1$ . For reference, we also show the late-reion-long-mfp model of Nasir & D’Aloisio (2019) (blue dashed curve) and the default reionization model of Keating et al. (2019) (magenta dotted curve). The  $2 - \sigma$  lower limits on  $Q_{\text{HII}}^{\text{V}}$  obtained using the dark pixel fraction (McGreer et al. 2015) are shown by green points with error-bars. The constraints we obtain are broadly in agreement with the reionization histories used in the existing simulations (Kulkarni et al. 2019; Keating et al. 2019; Nasir & D’Aloisio 2019) as well as the limits from the model-independent dark pixel fraction (McGreer et al. 2015). The allowed values of  $Q_{\text{HII}}^{\text{V}}$  are larger for the optimistic data set than the pessimistic one at  $z \geq 5.2$ . This is along the expected lines as the inferred values of  $\tau_{\text{eff}}$  for sight lines with no detections are larger in the pessimistic case, hence matching this data set requires more neutral patches in the IGM. The difference between the two data sets decrease at smaller  $z$  because of fewer non-detections.

At  $z = 5.4$ , the  $2 - \sigma$  upper limit on  $Q_{\text{HII}}^{\text{V}}$  is 0.99 (for both the data sets) while at the two lower redshifts the upper limits are consistent with unity. At  $z = 5.6$ , the corresponding  $2 - \sigma$  upper limit is  $\sim 0.95$ . This indicates that, in order to match the data at the  $2 - \sigma$  level, the completion of reionization must be delayed until  $z \sim 5.4$  (independent of how the non-detections are treated), i.e., the data are *not* consistent with complete reionization at  $z \gtrsim 5.6$ . Interestingly, the  $2 - \sigma$  lower limit on  $Q_{\text{HII}}^{\text{V}}$  at  $z = 5.2$  is 0.93 for the pessimistic data set, which would imply a rather significantly late completion of reionization. The constraints are rather poor at  $z = 6$  because of fewer sight lines; we nevertheless find that  $Q_{\text{HII}}^{\text{V}}$  can be as small as 0.4 if the pessimistic data set represents reality.

This statistical analysis shows the main benefit of our model. Given its computational efficiency, we can probe the parameter space in a reasonable amount of time and hence determine the range of histories allowed by the data. With improved data sets in the future, we can expect to test some of the model assumptions more critically and put more stringent constraints on reionization.

#### 4 SUMMARY AND DISCUSSION

Recent observations of the effective optical depth  $\tau_{\text{eff}}$  of Ly $\alpha$  absorption at  $5 \lesssim z \lesssim 6$  show significant fluctuations when averaged over reasonably large scales  $50h^{-1}\text{cMpc}$  scales. One possible interpretation of these observations is that the fluctuations arise because of left-over HI islands and that HI reionization is complete only at  $z \sim 5.2$  (Kulkarni et al. 2019; Keating et al. 2019; Nasir & D’Aloisio 2019). If this interpretation of the data is indeed true, it becomes imperative to include these observations in any parameter constraints related to the reionization history (in addition to, e.g., the existing CMB observations of electron scattering optical depth). Obtaining constraints, in turn, requires efficient methods of computing the relevant observables (in this case, the Ly $\alpha$  optical depth) so as to probe the space unknown parameters.

To achieve this goal, we have developed a semi-numerical technique to constrain the reionization history at  $5 \lesssim z \lesssim 6$ . Our method is appropriate for probing large-scale properties of the Ly $\alpha$  absorption in relatively low-

resolution simulation boxes and relies on two main inputs: (i) the modelling of ionized regions using a photon-conserving semi-numerical code of reionization (SCRIPT; Choudhury & Paranjape 2018) and (ii) modelling the Ly $\alpha$  optical depth using the fluctuating Gunn-Peterson approximation. To our knowledge, this is the least computationally expensive model to study the Ly $\alpha$  opacity fluctuations.

We find that the model is able to capture the essential properties of the HI field as observed in the Ly $\alpha$  absorption, similar to those found in more detailed simulations (Kulkarni et al. 2019; Keating et al. 2019; Nasir & D’Aloisio 2019). Since the method is computationally fast, it allows us to probe the parameter space quite efficiently and thus obtain the range of histories consistent with the data. We find that the inferred reionization history is delayed when we use the data set where non-detections of the flux are treated as having infinite optical depth (the so-called ‘pessimistic’ case of Bosman et al. 2018) compared to the case where non-detections are assumed to have optical depths just below the detection limit (the ‘optimistic’ case). At the  $2 - \sigma$  level, the data are *inconsistent* with reionization being complete at  $z \gtrsim 5.6$  (independent of which data set is used). The completion can be as late as  $z \sim 5.2$  if the pessimistic case represents reality, with the ionized volume fraction being possibly as low as 40% at  $z \sim 6$  for this case. The analysis thus indicates the potential of our technique in constraining reionization physics with more number of quasar sight lines at  $z \sim 6$ .

Upcoming quasar searches by surveys such as EUCLID (Euclid Collaboration et al. 2019; Griffin et al. 2020) and more efficient spectroscopic observations owing to the ELT (Gilmozzi & Spyromilio 2007) will significantly increase the amount and quality of Ly $\alpha$  opacity information at  $z > 6$  in the next decade. The discovery of bright quasars beyond  $z = 7.5$  (Bañados et al. 2018) ensures we will be able to map the large-scale evolution of opacity until  $z \sim 6.5$ , where Gunn-Peterson absorption is expected to saturate fully.

Obviously, fast semi-numerical models like ours often are unable to track all the physical processes self-consistently, thereby lacking predictive power. In this model, the main uncertainty arises from the treatment of the regions which do not receive photons from sources whose lines of sight pass through the HI islands, thus creating shadows and suppressing the photoionization rate. In the future, with a larger number of sight lines along  $z \sim 6$  quasars, it might be possible to take advantage of the fact that the model requires minimal computational time and constrain the free parameter which characterizes the uncertainty in the modelling these shadows.

In the future, we plan to further improve the analysis by including various effects which have been ignored in this work. The first is to model the Ly $\beta$  absorption from the same sight lines and compare with the available data (Eilers et al. 2019), thus obtaining more stringent constraints on the reionization history. The second is to forward model the noise in the observations and include it in the model, instead of considering the two extreme cases as done in this work. The third and perhaps most important improvement would be to self-consistently model the temperature evolution in each cell across redshifts. This would relax the assumption of the power law relation between the temperature and density of the cell and should be able to account for the depen-

dence of the temperature field on the reionization history. Such improvements, combined with the fact that the model is computationally inexpensive, would then allow for comparing with a wide variety of observations simultaneously and hence obtain constraints on reionization.

## ACKNOWLEDGEMENTS

TRC acknowledges support of the Department of Atomic Energy, Government of India, under project no. 12-R&D-TFR-5.02-0700 and the Associateship Scheme of ICTP. The research of AP is supported by the Associateship Scheme of ICTP, Trieste and the Ramanujan Fellowship awarded by the Department of Science and Technology, Government of India. SEIB acknowledges funding from the European Research Council (ERC) under the European Union's Horizon 2020 research and innovation program (grant agreement No. 669253).

## REFERENCES

- Bañados E., et al., 2018, *Nature*, **553**, 473
- Becker G. D., Bolton J. S., Madau P., Pettini M., Ryan-Weber E. V., Venemans B. P., 2015, *MNRAS*, **447**, 3402
- Boera E., Becker G. D., Bolton J. S., Nasir F., 2019, *ApJ*, **872**, 101
- Bolton J. S., Haehnelt M. G., 2007, *MNRAS*, **382**, 325
- Bolton J. S., Haehnelt M. G., Warren S. J., Hewett P. C., Mortlock D. J., Venemans B. P., McMahon R. G., Simpson C., 2011, *MNRAS*, **416**, L70
- Bosman S. E. I., Fan X., Jiang L., Reed S., Matsuoka Y., Becker G., Haehnelt M., 2018, *MNRAS*, **479**, 1055
- Calverley A. P., Becker G. D., Haehnelt M. G., Bolton J. S., 2011, *MNRAS*, **412**, 2543
- Chardin J., Haehnelt M. G., Aubert D., Puchwein E., 2015, *MNRAS*, **453**, 2943
- Chardin J., Puchwein E., Haehnelt M. G., 2017, *MNRAS*, **465**, 3429
- Chardin J., Haehnelt M. G., Bosman S. E. I., Puchwein E., 2018, *MNRAS*, **473**, 765
- Choudhury T. R., Ferrara A., 2005, *MNRAS*, **361**, 577
- Choudhury T. R., Paranjape A., 2018, *MNRAS*, **481**, 3821
- Croft R. A. C., Weinberg D. H., Katz N., Hernquist L., 1998, *ApJ*, **495**, 44
- D'Aloisio A., McQuinn M., Trac H., 2015, *ApJ*, **813**, L38
- Davies F. B., Furlanetto S. R., 2016, *MNRAS*, **460**, 1328
- Davies F. B., Hennawi J. F., Eilers A.-C., 2020, *MNRAS*, **493**, 1330
- Dixon K. L., Furlanetto S. R., 2009, *ApJ*, **706**, 970
- Durovčíková D., Katz H., Bosman S. E. I., Davies F. B., Devriendt J., Slyz A., 2020, *MNRAS*,
- Eilers A.-C., Davies F. B., Hennawi J. F., Prochaska J. X., Lukić Z., Mazzucchelli C., 2017, *ApJ*, **840**, 24
- Eilers A.-C., Davies F. B., Hennawi J. F., 2018a, *ApJ*, **864**, 53
- Eilers A.-C., Hennawi J. F., Davies F. B., 2018b, *ApJ*, **867**, 30
- Eilers A.-C., Hennawi J. F., Davies F. B., Oñorbe J., 2019, *ApJ*, **881**, 23
- Euclid Collaboration et al., 2019, *A&A*, **631**, A85
- Fan X., et al., 2000, *AJ*, **120**, 1167
- Fan X., et al., 2001, *AJ*, **122**, 2833
- Fan X., Narayanan V. K., Strauss M. A., White R. L., Becker R. H., Pentericci L., Rix H.-W., 2002, *AJ*, **123**, 1247
- Fan X., et al., 2003, *AJ*, **125**, 1649
- Fan X., et al., 2004, *AJ*, **128**, 515
- Fan X., et al., 2006a, *AJ*, **131**, 1203
- Fan X., et al., 2006b, *AJ*, **132**, 117
- Foreman-Mackey D., Hogg D. W., Lang D., Goodman J., 2013, *PASP*, **125**, 306
- Friedrich M. M., Mellema G., Alvarez M. A., Shapiro P. R., Iliev I. T., 2011, *MNRAS*, **413**, 1353
- Gaikwad P., Choudhury T. R., Srianand R., Khaire V., 2018, *MNRAS*, **474**, 2233
- Gaikwad P., et al., 2020, arXiv e-prints, p. arXiv:2001.10018
- Gallerani S., Choudhury T. R., Ferrara A., 2006, *MNRAS*, **370**, 1401
- Gallerani S., Ferrara A., Fan X., Choudhury T. R., 2008, *MNRAS*, **386**, 359
- Gilmozzi R., Spyromilio J., 2007, *The Messenger*, **127**, 11
- Goodman J., Weare J., 2010, *Communications in Applied Mathematics and Computational Science*, **5**, 65
- Greig B., Mesinger A., 2015, *MNRAS*, **449**, 4246
- Greig B., Mesinger A., Haiman Z., Simcoe R. A., 2017, *MNRAS*, **466**, 4239
- Greig B., Mesinger A., Bañados E., 2019, *MNRAS*, **484**, 5094
- Griffin A. J., Lacey C. G., Gonzalez-Perez V., Lagos C. d. P., Baugh C. M., Fanidakis N., 2020, *MNRAS*, **492**, 2535
- Hinshaw G., et al., 2013, *ApJS*, **208**, 19
- Hutter A., 2018, *MNRAS*, **477**, 1549
- Jenkins A., Frenk C. S., White S. D. M., Colberg J. M., Cole S., Evrard A. E., Couchman H. M. P., Yoshida N., 2001, *MNRAS*, **321**, 372
- Keating L. C., Kulkarni G., Haehnelt M. G., Chardin J., Aubert D., 2019, arXiv e-prints, p. arXiv:1912.05582
- Kulkarni G., Keating L. C., Haehnelt M. G., Bosman S. E. I., Puchwein E., Chardin J., Aubert D., 2019, *MNRAS*, **485**, L24
- Maselli A., Gallerani S., Ferrara A., Choudhury T. R., 2007, *MNRAS*, **376**, L34
- McGreer I. D., Mesinger A., Fan X., 2011, *MNRAS*, **415**, 3237
- McGreer I. D., Mesinger A., D'Odorico V., 2015, *MNRAS*, **447**, 499
- Meiksin A., 2020, *MNRAS*, **491**, 4884
- Mitra S., Choudhury T. R., Ferrara A., 2011, *MNRAS*, **413**, 1569
- Mitra S., Choudhury T. R., Ferrara A., 2012, *MNRAS*, **419**, 1480
- Mitra S., Ferrara A., Choudhury T. R., 2013, *MNRAS*, **428**, L1
- Mitra S., Choudhury T. R., Ferrara A., 2018, *MNRAS*, **473**, 1416
- Nasir F., D'Aloisio A., 2019, arXiv e-prints, p. arXiv:1910.03570
- Paranjape A., Choudhury T. R., Padmanabhan H., 2016, *MNRAS*, **460**, 1801
- Planck Collaboration et al., 2014, *A&A*, **571**, A16
- Planck Collaboration et al., 2019, arXiv e-prints, p. arXiv:1907.12875
- Pritchard J. R., Loeb A., Wyithe J. S. B., 2010, *MNRAS*, **408**, 57
- Puchwein E., Bolton J. S., Haehnelt M. G., Madau P., Becker G. D., Haardt F., 2015, *MNRAS*, **450**, 4081
- Raskutti S., Bolton J. S., Wyithe J. S. B., Becker G. D., 2012, *MNRAS*, **421**, 1969
- Sheth R. K., Tormen G., 2002, *MNRAS*, **329**, 61
- Songaila A., 2004, *AJ*, **127**, 2598
- Songaila A., Cowie L. L., 2002, *AJ*, **123**, 2183
- Springel V., 2005, *MNRAS*, **364**, 1105
- Worseck G., et al., 2014, *MNRAS*, **445**, 1745
- Wyithe J. S. B., Bolton J. S., 2011, *MNRAS*, **412**, 1926
- Wyithe J. S. B., Loeb A., 2003, *ApJ*, **586**, 693
- Wyithe J. S. B., Loeb A., 2004, *Nature*, **427**, 815
- Zahn O., Lidz A., McQuinn M., Dutta S., Hernquist L., Zaldarriaga M., Furlanetto S. R., 2007, *ApJ*, **654**, 12

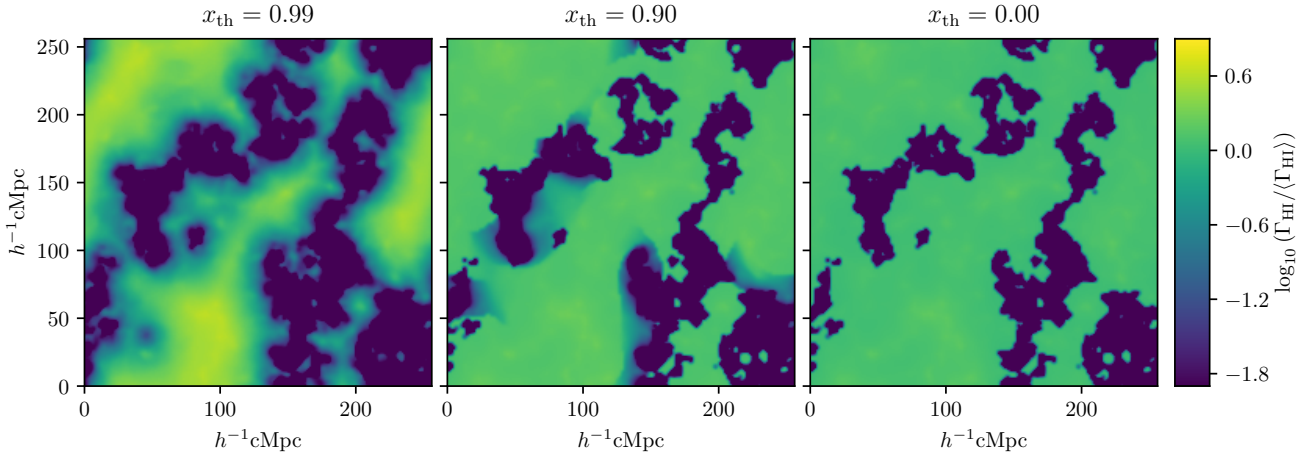


**Figure A1.** The two-dimensional maps of the photoionization rate fluctuations for a slice of thickness  $2h^{-1}\text{cMpc}$  at  $z = 5.8$  for different values of  $x_{\text{th}}$  as mentioned above the respective panels.

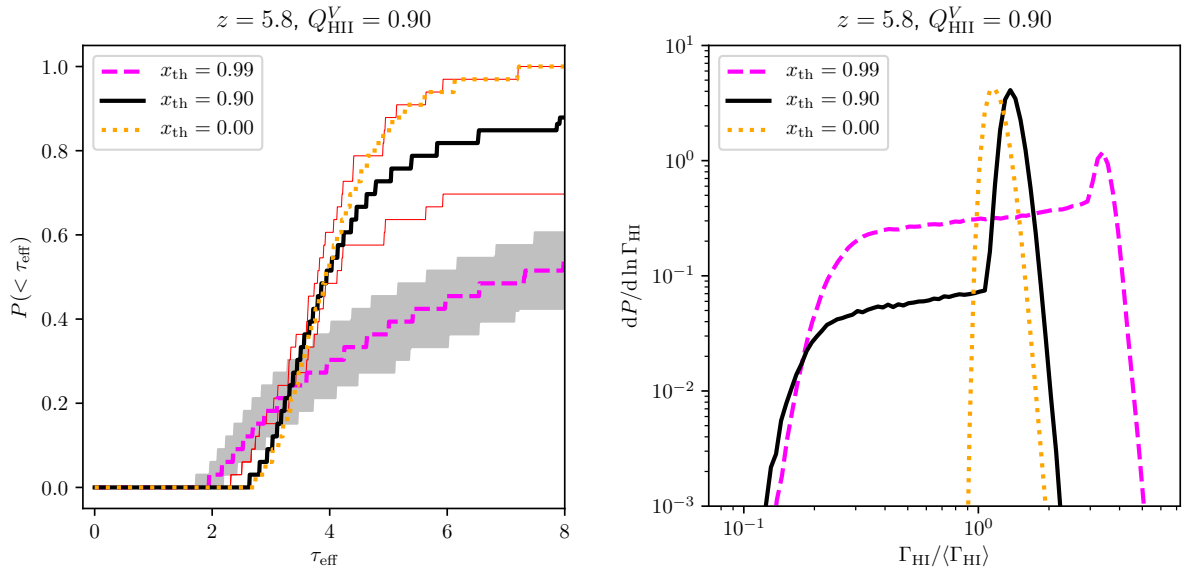


**Figure A2.** The left panel shows the  $\tau_{\text{eff}}$  CDF for three values of  $x_{\text{th}}$  at  $z = 5.8$  (with red curves showing the optimistic and pessimistic data sets used in the paper). The right panel shows the corresponding PDFs of the photoionization rate *in the ionized regions*.

## APPENDIX A: DEPENDENCE OF THE RESULTS ON THE PARAMETER CHOICES

In this appendix, we discuss the dependence of our model on different parameters once we vary them beyond their default values.

### A1 Varying $x_{\text{th}}$ : effect of shadows

The first parameter considered is the threshold ionized fraction  $x_{\text{th}}$  chosen to identify the spherically averaged ionized bubbles. Recall that we have taken the default value of this parameter as  $x_{\text{th}} = 0.9$ . We show the maps of photoionization rates for three different values of  $x_{\text{th}}$  in Figure A1. We can see that as the value of  $x_{\text{th}}$  increases, the fields tend to contain more shadow-like structures in the ionized regions

which lie close to the neutral regions. These shadows are points where  $\Gamma_{\text{HI}}$  is lower because they do not receive photons from the direction of the neutral regions.

As  $x_{\text{th}} \rightarrow 1$  (the left hand panel), only those spheres which consist of completely ionized pixels would be identified as ionized. As a result, the scale  $\lambda_{\text{bub}}$  above which the pixel under consideration encounters neutral cells become relatively smaller (assuming all the other conditions to remain the same). This leads to the prominence of the shadows as seen in the plot. On the other extreme, as  $x_{\text{th}} \rightarrow 0$  (the right hand panel), the  $\lambda_{\text{bub}}$  can be as large as the box size, hence the shadows are absent.

The presence of the shadows would lead to larger fluctuations in the photoionization rate  $\Gamma_{\text{HI}}$  and hence the  $\tau_{\text{eff}}$  distribution would be wider. We show the  $\tau_{\text{eff}}$  CDF in the

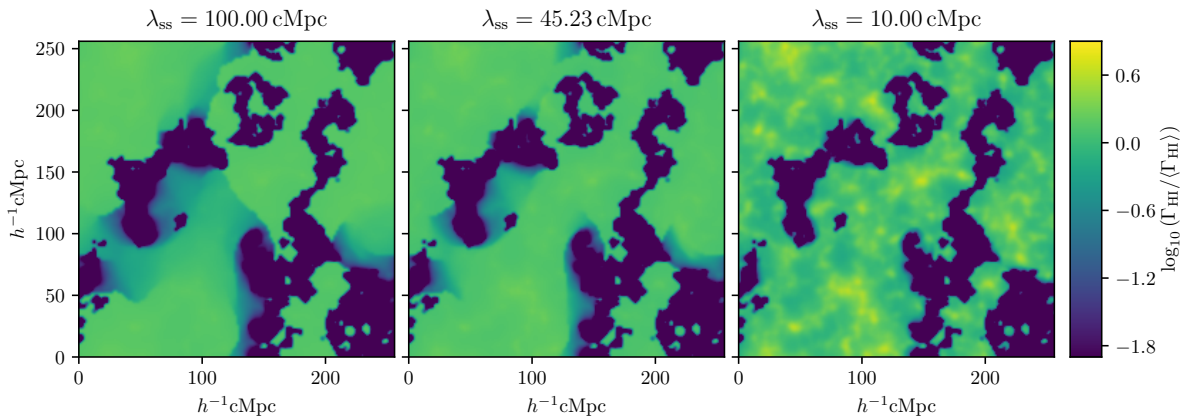


**Figure A3.** Same as Figure A1 but for different values of  $\lambda_{\text{ss}}$ .

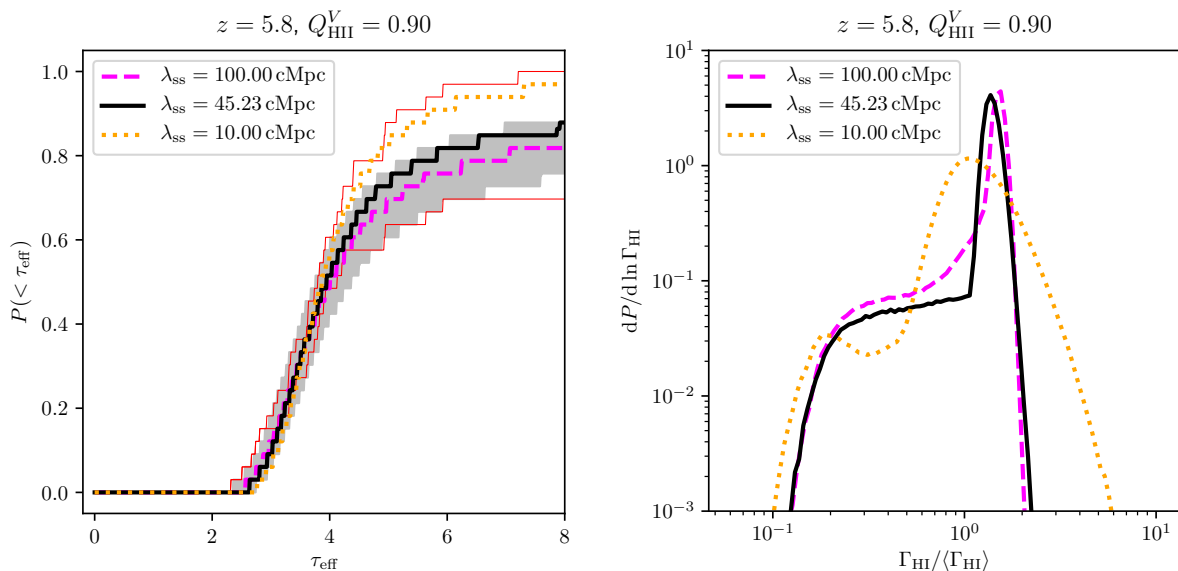


**Figure A4.** Same as Figure A2 but for different values of  $\lambda_{\text{ss}}$ .

left panel of Figure A2 for three different values of  $x_{\text{th}}$ . The redshift is chosen to be  $z = 5.8$  and the volume-averaged ionized fraction is  $Q_{\text{HII}}^V = 0.9$ . One can clearly see that higher values of  $x_{\text{th}}$  lead to wider CDF, as expected. The  $\Gamma_{\text{HI}}$  distribution (considering only the ionized regions) too becomes wider with increasing  $x_{\text{th}}$  as can be seen from the right hand panel of Figure A2. In particular, the model with  $x_{\text{th}} = 0.99$  shows a prominent “knee” at low  $\Gamma_{\text{HI}}$  which indicates substantial presence of the shadows near the neutral regions. Such shadows are completely absent for the other extreme case with  $x_{\text{th}} = 0$ .

From the above discussion, it is clear that if we choose a higher than default value of  $x_{\text{th}} = 0.9$ , we would require a relatively more ionized IGM to match the observed  $\tau_{\text{eff}}$  distribution. In such a case, a small number of neutral regions would create sufficient shadow-like structures so as to produce the required  $\Gamma_{\text{HI}}$  fluctuation. Obviously, for smaller  $x_{\text{th}}$ , the  $Q_{\text{HII}}^V$  required to match the data would be smaller. In fact, the reason for choosing the default  $x_{\text{th}}$  in the pa-

per should also be clear from this discussion. Had we chosen a higher (lower) value, matching the data would require ionized fractions much larger (smaller) than what is found in the simulations of Kulkarni et al. (2019); Keating et al. (2019); Nasir & D’Aloisio (2019). We found that  $x_{\text{th}}$  values between 0.8 and 0.9 give reionization histories consistent with the other works.

It is worth noting a caveat to the above discussion, namely, it is unclear if the choice of  $x_{\text{th}}$  depends on the reionization history used. Verifying this would require more robust calibration to the full radiative transfer simulations which we plan to explore elsewhere.

## A2 The mean free path $\lambda_{\text{ss}}$

The default value of the mean free path  $\lambda_{\text{ss}}$  determined by the distance between the self-shielded regions has been chosen as the value extrapolated from lower redshift observa-

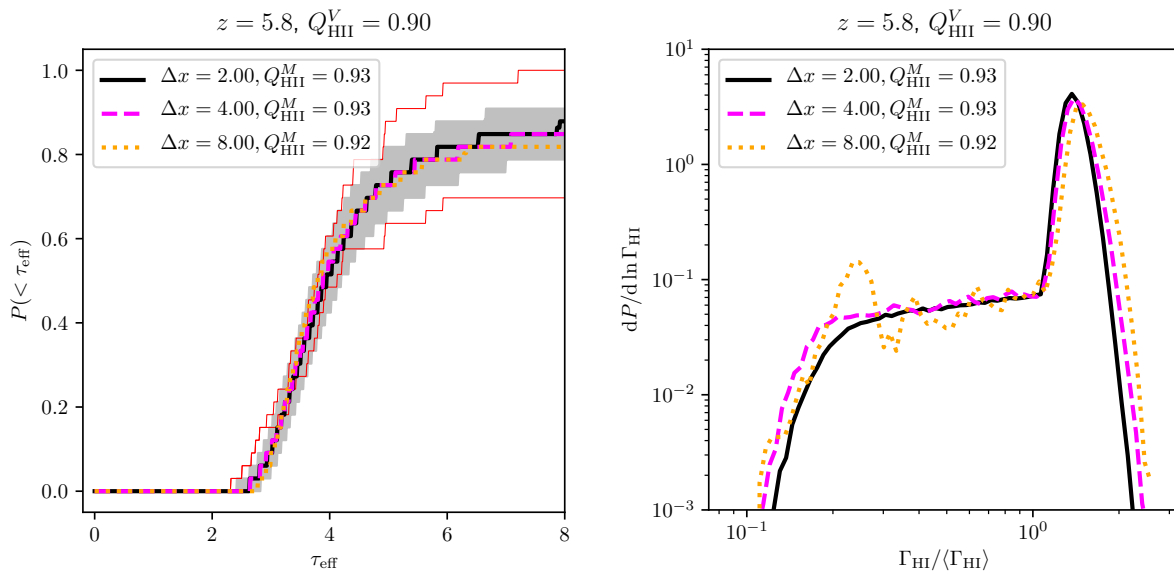


**Figure A5.** Same as Figure A2 but for different resolutions used while generating the HI field and the Ly $\alpha$  optical depth.

tions. We vary the value to two extremes as see the effect on the observable considered in the paper.

We compare the  $\Gamma_{\text{HI}}$  maps for different values of  $\lambda_{\text{ss}}$  in Figure A3. In the left hand panel, we choose a high value  $\lambda_{\text{ss}} = 100\text{cMpc}$  which essentially implies that points in the ionized regions can see sources at large distances (unless blocked by a neutral region). Since the effective mean free path  $\lambda_{\text{mfp}}$  is the minimum of  $\lambda_{\text{ss}}$  and  $\lambda_{\text{bub}}$ , it is determined by  $\lambda_{\text{bub}}$  for such large values of  $\lambda_{\text{ss}}$ . As a result, we can see the shadows even at substantial distances from the neutral boundaries. Thus we end up with a somewhat counter-intuitive result where increasing  $\lambda_{\text{ss}}$  leads to more large-scale fluctuations in  $\Gamma_{\text{HI}}$ . Physically, for large  $\lambda_{\text{ss}}$ , only points that are considerably far away from the islands (say, with distances  $\gtrsim \lambda_{\text{ss}}$ ) can receive photons from all directions without being obstructed by the islands. Hence the number of points that are affected by these islands are relatively larger thus leading to more fluctuations.

In the right panel, we show the  $\Gamma_{\text{HI}}$  map for a smaller value  $\lambda_{\text{ss}} = 10\text{cMpc}$ . As expected, we find a lot of small-scale fluctuations in  $\Gamma_{\text{HI}}$  in this case. Also, only points that are very close to the islands ( $\lesssim 10\text{cMpc}$ ) are affected by them leading to a much smaller effect of the shadows.

The effect of  $\lambda_{\text{ss}}$  on the  $\tau_{\text{eff}}$  CDF is shown in the left panel of Figure A4, while the right panel shows the  $\Gamma_{\text{HI}}$  PDF. As expected, the  $\tau_{\text{eff}}$  CDF is wider for larger  $\lambda_{\text{ss}}$  because of more large-scale fluctuations, and similarly narrower for smaller  $\lambda_{\text{ss}}$ . However, the variation even in such extreme cases is within the cosmic variance of the observable, and well within the limits set by the pessimistic and optimistic cases. Hence for the purpose of this work,  $\lambda_{\text{ss}}$  has a much less effect on the modelling. Interestingly, the  $\Gamma_{\text{HI}}$  distribution for  $\lambda_{\text{ss}} = 10\text{cMpc}$  looks quite different from the other two cases. The knee-like part is almost absent because there are no shadows in the ionized regions. However, the small  $\lambda_{\text{ss}}$  does increase the width the distribution as the small-scale (i.e., around the grid scale) fluctuations are larger. However,

these average out at  $50h^{-1}\text{cMpc}$  scales and do not matter in the  $\tau_{\text{eff}}$  distribution.

### A3 Convergence with respect to resolution

In this section, we study the dependence of our results on the grid size chosen for generating the ionized bubbles and computing the Ly $\alpha$  optical depth. While comparing the results for different resolutions, we compare them at the same value of  $Q_{\text{HII}}^V$  as the Ly $\alpha$  absorption is most sensitive to this parameter. Also note that while obtaining the  $\tau_{\alpha}$  at the grid cells, we normalize the values so as to obtain the same observed mean transmitted flux.

The  $\tau_{\text{eff}}$  CDF  $P(< \tau_{\text{eff}})$  and the  $\Gamma_{\text{HI}}$  PDF  $dP/d \ln \Gamma_{\text{HI}}$  for different grid sizes are shown in the left and right panels of Figure A5 respectively. We can clearly see that  $P(< \tau_{\text{eff}})$  is almost identical for the three cases, indicating that our results are not sensitive to the grid size we choose in the range  $2h^{-1}\text{cMpc} \leq \Delta x \leq 8h^{-1}\text{cMpc}$ . It is important to stress once more that these curves have been obtained by normalizing the Ly $\alpha$  optical depth so as to obtain the same effective optical depth. The normalization constant varies across the resolution used, however, the resulting  $P(< \tau_{\text{eff}})$  remains the same. This is expected as the effective optical depth is affected by the small-scale high-density regions that depend on the resolution used.

The  $\Gamma_{\text{HI}}$  PDF, shown in the right panel, too is almost identical for different resolutions. The coarse resolution simulation shows some noisy behaviour at low  $\Gamma_{\text{HI}}$  (in the knee corresponding to the shadows) because of less number of points. Overall though we can safely conclude that our results are not sensitive to the resolution. We use  $\Delta x = 4h^{-1}\text{cMpc}$  for the MCMC analysis in the paper.